# Sparse and Low-Rank Decomposition of a Hankel Structured Matrix for Impulse Noise Removal

Kyong Hwan Jin and Jong Chul Ye, *Senior Member, IEEE*

*Abstract*—Recently, the annihilating filter-based low-rank Hankel matrix (ALOHA) approach was proposed as a powerful image inpainting method. Based on the observation that smoothness or textures within an image patch corresponds to sparse spectral components in the frequency domain, ALOHA exploits the existence of annihilating filters and the associated rank-deficient Hankel matrices in an image domain to estimate any missing pixels. By extending this idea, here we propose a novel impulse-noise removal algorithm, which uses the sparse and low-rank decomposition of a Hankel structured matrix. This method, referred to as the robust ALOHA, is based on the observation that an image corrupted with impulse noise has intact pixels; consequently, the impulse noise can be modeled as sparse components, whereas the underlying image can still be modelled using a low-rank Hankel structured matrix. To solve the sparse and low-rank matrix decomposition problem, we propose an alternating direction method of multiplier (ADMM) approach, with initial factorized matrices coming from a low-rank matrix-fitting (LMaFit) algorithm. To adapt local image statistics that have distinct spectral distributions, the robust ALOHA is applied in a patch-by-patch manner. Experimental results from impulse noise for both single-channel and multichannel color images demonstrate that the robust ALOHA is superior to existing approaches, especially during the reconstruction of complex texture patterns.

*Index Terms*—Annihilating filter, sparse and low rank decomposition, Impuse noise, Hankel matrix, ADMM, salt/pepper noise, robust principal component analysis (RPCA)

## I. INTRODUCTION

Impulse noise occurs as a result of a malfunction of detector pixels in a camera or from missing memory elements in imaging hardware [1]. There are two types of impulse noise. The first includes salt/pepper noise that

The authors are with Dept. of Bio and Brain Engineering, KAIST, Daejeon 305-701, Republic of Korea. (Email:jong.ye@kaist.ac.kr). The first author is currently a member of Biomedical Imaging Group, École Polytechnique Fédérale de Lausanne (EPFL), Switzerland.

This paper has supplementary downloadable material available at http://ieeexplore.ieee.org., provided by the author. The material includes Appendix referred by this paper. Contact [jong.ye@kaist.ac.kr] for further questions about this work.

match the extreme dynamic range of a pixel value. In this case, noisy pixels can be relatively easily detected by an adaptive median filter (AMF) [2]. The second example involves random-valued impulse noise (RVIN), which occur accidentally within the dynamic range of an image pixel. Unlike the salt/pepper noise, RVIN cannot be effectively detected by an adaptive median filter. Instead, an adaptive center-weighted median filter (ACWMF) [3] has been widely used to identify noisy pixels. Even with AMF and ACWMF, when the density of the noise increases, the denoising performance of these single-step algorithms becomes severely degraded. To address this weakness, two-phase denoising algorithms with a "decision-based filter" or a "switching filter" have been proposed [1], [4]–[7]. More specifically, these algorithms consist of two parts: the detection of noise pixels by AMF, ACWMF, boundary discriminative noise detection (BDND) [7], or by other outlier finding algorithms, followed by the replacement of those pixels with estimated values using the total variation method [4] or edge preserving regularization steps [1], [8], while leaving other noiseless pixels unchanged.

On the other hand, impulse-noise denoising algorithms using proximal optimizations with non-smooth penalties have been proposed recently [9]–[11]. In particular, in the TVL1 (total variation $l_1$) approach [9], [10], the data fidelity term was measured using the $l_1$ norm dealing with impulse outliers, and total variation regularization was used as the image smoothness penalty. The algorithm can effectively remove impulse noise at sufficiently rapid speed. However, the algorithm often causes edge distortions or texture pattern blurring due to the TV term. With the advance of compressed sensing (CS) theory, impulse-noise denoising methods based on compressed sensing have also been proposed [12], [13]. In one study [13], the authors encouraged the use of spatio-spectral domain redundancy using a blind compressed sensing framework. This approach demonstrated outstanding recovery performance; however, the algorithm could not be used without a highly correlated spectral dataset. In another study [12], the sparsity level of a single image was used as a minimization criterion, just as in the conventional CS approach. However, the performance was

inferior to those by the two-phase methods [1]. Although a low-rank matrix completion approach for impulse noise denoising for video sequences was proposed [14], the algorithm only worked for video sequence denoising. Meanwhile, the matrix decomposition methods even with outliers were proposed [15], [16].

There are several types of noise in images such as Gaussian, Poisson, or impulse noise. Gaussian noise is independently generated for most pixels from thermal noise during electronics measurements. Poisson noise arises from many applications, where data are collected by counting a series of discrete events, such as photons. The noise variance of Poisson noise is equal to the mean intensity value such that most of the pixels are essentially contaminated with noise. On the other hand, one of the unique characteristics of impulse noise is that an image corrupted with impulse noise still has intact pixels. Accordingly, the impulse noise can be modeled as sparse components, whereas the underlying intact image retains the original image characteristics. In fact, this was the main idea utilized in the TVL1 approach [10], which is also employed in this paper. However, instead of using TV image modeling, we employ a state-of-the-art image-modeling technique using a Hankel structured low-rank matrix. Specifically, inspired by our novel image-inpainting method using a structured low-rank matrix [17]–[21], one of the most important contributions of this paper is to demonstrate that the impulse noise removal problem can be formulated as a *sparse and low-rank* decomposition problem of a structured Hankel matrix.

More specifically, in our previous study [17], we demonstrated that a smooth, edged or textured image-patch leads to a *sparse* spectrum in the frequency domain. Thus, the sampling theory of signals with a finite rate of innovations (FRI) [22] tells us that there exists annihilating filters that eliminate the pixel values within the corresponding image patch. Moreover, the existence of the annihilating filter enables us to construct a rank-deficient Hankel structured matrix whose rank is determined by the sparsity level in the spectral domain [17], [18]. Given this observation, an image patch can be modeled using an annihilating filter-based low-rank Hankel matrix (ALOHA), with the image-inpainting problem solved using a low-rank matrix completion algorithm. This idea was extended by our group to examine compressed sensing MRI [19]–[21], image deconvolution [23], and the interpolation of scanning microscopy [24]. Ongie *et al.* independently developed similar approaches for super-resolution MRI [25]. Similar extensions were also addressed in Qu et al [26] and Cai et al [27].

While the image-inpainting problem is closely related to the impulse noise removal problem, there exists a fundamental difference between image inpainting and impulse denoising problems. Specifically, in the impulse-noise removal problem, we do not know the locations of noise *a priori* such that they must be estimated as well. On the other hand, in the image-inpainting problem [17], the missing pixel locations are known *a priori* and we only need to estimate the missing pixel values. Therefore, impulse-noise removal problems are much more difficult than image-inpainting problems and are often described as "blind inpainting" [4], [28], [29].

In fact, one of the most important observations is that the construction of a Hankel structured matrix is a *linear* lifting scheme such that the sparse components in an image are also sparse in the lifted Hankel matrix. Therefore, we can use a sparse and low-rank decomposition of the Hankel structured matrix to decouple the sparse impulse noise components from the underlying image. The new algorithm, what we call robust ALOHA, is applied in a patch-by-patch manner to adapt to local image statistics that have a distinct spectral distribution. To solve the associated sparse and low-rank decomposition problem of a Hankel structure matrix, an alternating direction method of multiplier (ADMM) [30] is utilized with the initial factorized matrices from the low-rank matrix-fitting algorithm (LMaFit) [31]. Furthermore, the denoising algorithm is also extended to exploit the joint sparsity constraint in color images by stacking a Hankel structured matrix from each channel side by side and applying sparse and low-rank decomposition to the concatenated Hankel matrix. Using extensive numerical experiments, we demonstrate that the robust ALOHA significantly improves the image quality.

We are aware that there has been significant progress on the decomposition of superposed matrices consisting of low-rank and sparse components [32], [33], often called robust principal component analysis (RPCA) [32]. However, the matrix in RPCA is usually unstructured, whereas robust ALOHA uses a Hankel structured matrix. As will be shown later, the lifting to a Hankel structured matrix significantly improves the denoising performance by exploiting the spectral domain sparsity, even when compared to the locally adapted RPCA framework using local patches [28].

## II. THEORY

### A. Review of the TVL1 approach

Because impulse noise occur due to the malfunctioning of detector or memory elements [1], only a subset of image pixels are corrupted by noise. Therefore, if $\mathbf{M}$ denotes an image measurement corrupted by impulse

noise, it can be modeled as

$$\mathbf{M} = \mathbf{X} + \mathbf{E}$$

where $\mathbf{X}$ is the underlying "clean" image and $\mathbf{E}$ denotes a sparse matrix composed of impulse noise. This model is quite often used in the existing impulse-noise removal algorithms. For example, in TVL1 [9], [10], $\mathbf{E}$ is considered as a sparse outlier, whereas the underlying image is designed to have a minimum total variations. This leads to the following cost function:

$$\|\mathbf{M} - \mathbf{X}\|_1 + \lambda TV(\mathbf{X}) \qquad (1)$$

where the $\|\cdot\|_1$ norm is the $l_1$ norm corresponding to the summation of the absolute values of each matrix element for outlier removal, and the $TV(\mathbf{X})$ denotes the 2-D TV penalty in the modelling of the underlying image. In the following paragraphs, we explain how the image model in Eq. (1) can be modified in the proposed method to give superior denoising performance.
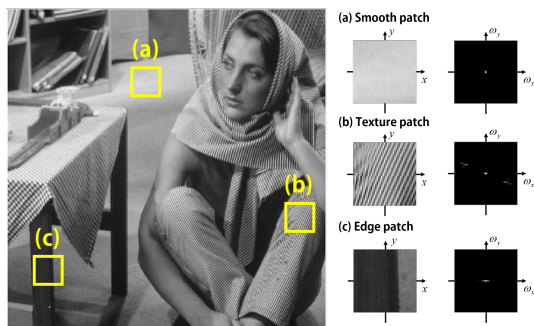


Fig. 1. Spectral components of patches from (a) smooth background, (b) texture, and (c) edge.

### B. Image modelling using a low-rank Hankel structured matrix

In our recent work [17], we demonstrate that diffusion [34] and/or Gaussian Markov random field (GMRF) approaches for image modelling [35] are closely related to an annihilating filter relationship from the sampling theory of signals with a finite rate of innovations (FRI) [22]. More specifically, as shown in Fig. 1(a), a smoothly varying patch usually has spectrum content in the low-frequency regions, while the other frequency regions have very few spectral components. Similar spectral domain sparsity can be observed in the texture patch shown in Fig. 1(b), where the spectral components are mainly concentrated on the fundamental frequencies of the patterns. For the case of an abrupt transition along the edge as shown in Fig. 1(c), the spectral components are mostly localized along the $\omega_x$ axis.

Specifically, when an image patch $x[\mathbf{n}]$ in discrete domain has sparse *spectral* components in continuous Fourier domain (i.e. in $\mathbb{R}^2$), we can show that there exists a corresponding annihilating filter in the *image* domain. More specifically, let the sparse spectral components be modeled as peoriodic stream of 2-D Diracs:

$$\hat{x}(\boldsymbol{\omega}) := \hat{x}(\omega_x, \omega_y) \qquad (2)$$

$$= 2\pi \sum_{m,n\in\mathbb{Z}} \sum_{j=0}^{k-1} c_j \delta(\omega_x - \omega_{x,j} - m\pi, \omega_y - \omega_{y,j} - n\pi),$$

where $\{(\omega_{x_i}, \omega_{y_i})\}_{i=1}^{k}$ denote the location of non-zero spectral components and $k$ denotes the number of non-zero spectral components. Then, the corresponding image domain signal is discrete and given by

$$x[\mathbf{n}] := x[m,n] = \sum_{j=0}^{k-1} c_j e^{i(\omega_{x_j} m + \omega_{y_j} n)} . \qquad (3)$$

We now construct a $p_1 \times q_1$- filter $h[m,n]$ whose z-tranform is given by

$$h(z_1, z_2) = \prod_{j=0}^{k-1} \left(1 - e^{i(\omega_{x_j} m + \omega_{y_j} n)} (z_1 z_2)^{-1}\right) , \quad (4)$$

such that the corresponding filter $h[m,n]$ annihilates the patch image $x[m,n]$:

$$(h * x)[m,n] = \sum_{j=0}^{k-1} c_j \underbrace{\left(\sum_{p=0}^{p_1-1} \sum_{q=0}^{q_1-1} h[p,q] u_j^{-p} v_j^{-q}\right)}_{h(u_j, v_j)} u_j^m v_j^n = 0 \quad (5)$$

where $u_j = e^{i\omega_{x_j}}$ and $v_j = e^{i\omega_{y_j}}$. Then, the following theorem says that a 2-D Hankel structured matrix of the image patch is low-ranked.

**Theorem 1.** *Let a $p_1 \times q_1$-size filter $h[m,n]$ denote a minimum size annihilating filter that annihilates $x[m,n]$. Then, for an $M \times N$ patch area $\mathbf{X} = \{x[m,n]\}_{m,n=1}^{M,N}$, $\mathscr{H}(\mathbf{X})$ denotes a 2-D Hankel structured matrix given by*

$$\begin{bmatrix} \mathscr{H}_{1d}(\mathbf{x}_1) & \mathscr{H}_{1d}(\mathbf{x}_2) & \cdots & \mathscr{H}_{1d}(\mathbf{x}_q) \\ \mathscr{H}_{1d}(\mathbf{x}_2) & \mathscr{H}_{1d}(\mathbf{x}_3) & \cdots & \mathscr{H}_{1d}(\mathbf{x}_{q+1}) \\ \vdots & \vdots & \ddots & \vdots \\ \mathscr{H}_{1d}(\mathbf{x}_{N-q+1}) & \mathscr{H}_{1d}(\mathbf{x}_{N-q+2}) & \cdots & \mathscr{H}_{1d}(\mathbf{x}_N) \end{bmatrix}, \quad (6)$$

*and a 1-D Hankel matrix $\mathscr{H}_{1d}(\mathbf{x}_i)$ for the i-th column vector $\mathbf{x}_i$ of the matrix $\mathbf{X}$ is given by*

$$\begin{bmatrix} x[1,i] & x[2,i] & \cdots & x[p,i] \\ x[2,i] & x[3,i] & \cdots & x[p+1,i] \\ \vdots & \vdots & \ddots & \vdots \\ x[M-p+1,i] & x[M-p+2,i] & \cdots & x[M,i] \end{bmatrix}.$$

*where $\min\{M-p+1, p\} > p_1, \min\{N-q+1, q\} > q_1$.*

*Then we have*

$$\text{RANK}\mathscr{H}(\mathbf{X}) \le pq - (p - p_1)(q - q_1). \tag{7}$$

*Proof.* See Appendix A in Supplementary Material. □

Due to the construction of a $p_1 \times q_1$- annihilating filter using z-transform in (4), we can easily see that $\max\{p_1, q_1\} \le k$, where $k$ denotes the numbers of non-zero spectral components. Thus, Eq. (7) can be converted to

$$\text{RANK}\mathscr{H}(\mathbf{X}) \le pq - (p - p_1)(q - q_1) \le k(p + q - k).$$

Consequently, for a sufficiently small $k$, we can see that $\text{RANK}\mathscr{H}(\mathbf{X})$ is much smaller than the number of column, and $\mathscr{H}(\mathbf{X})$ is low-ranked. Based on the observation, in our previous work [17], we demonstrated that the missing pixels in an image can be inpainted by using a low-rank Hankel structured matrix completion approach. Related mathematical theory including near optimal performance guarantee for a convex approach using nuclear norm minimization can be also found in our recent theoretical work [18]. In this paper, this approach will be recasted into sparse and low-rank decomposition for impulse-noise removal.

### C. Sparse + Low-rank Decomposition Model for Hankel Structured Matrix from Impulse noise
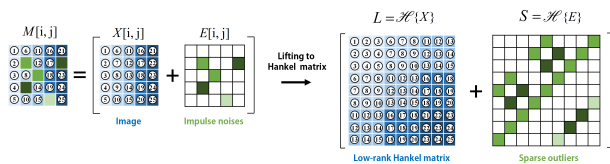


Fig. 2. Sparse + low rank decomposition of Hankel structured matrix from an image patch corrupted with impulse noise. Because a lifting to Hankel structure is linear, the sparse impulse noise are also lifted to sparse outliers.

Unlike the lifting scheme used for phase-retrieval problems [36], our lifting scheme involving a Hankel structured matrix is *linear* such that additive sparse impulse-noise is also lifted to sparse outliers in the lifted Hankel structured matrix (see Figure 2). Accordingly, if an underlying image is corrupted with sparse impulse noise, then we have

$$\mathscr{H}(\mathbf{X}) = \mathbf{L} + \mathbf{S} \tag{8}$$

where $\mathbf{L}$ denotes the low-rank component and $\mathbf{S}$ represents the sparse components originating from impulse noise, which are both in the Hankel structures. This is the key property we want to exploit in our impulse-noise removal algorithm. In fact, to address this type of sparse

+ low-rank decomposition, robust principal component analysis (RPCA) was actively investigated [32], [33]. More specifically, for a given measurement matrix $\mathbf{M}$, the RPCA solves the following minimization problem:

$$\min \quad \|\mathbf{L}\|_* + \tau\|\mathbf{S}\|_1 \tag{9}$$

$$\text{subject to} \quad \mathbf{L} + \mathbf{S} = \mathbf{M}, \tag{10}$$

where $\|\cdot\|_*$ denotes the nuclear norm. To minimize this, alternating direction methods were employed.

Compared to the standard RPCA approach, our sparse + low-rank decomposition problem using (8) requires an additional constraint due to the Hankel structure. Therefore, the RPCA algorithm should be modified. The specific optimization algorithm under this constraint will be explained later. Additionally, because the image statistics change across an image with spatially varying annihilating properties, a noisy image should be partitioned into overlapped patches, which are processed independently in a patch-by-patch fashion using robust ALOHA with their average reconstruction pixel values used as described in the algorithm flowchart shown in Fig. 3.
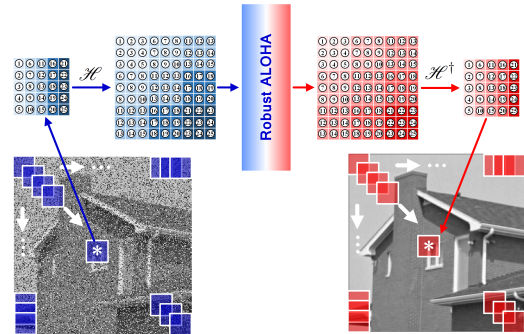


Fig. 3. Patch-by-patch processing framework using robust ALOHA for impulse noise removal.

### III. OPTIMIZATION METHODS

### A. Sparse + Low-rank Decomposition of a Hankel Matrix

Note that the Hankel structured matrix in (6) is determined by the underlying image patch ($\mathbf{X}$) size and the associated annihilating filter ($\mathbf{H}$) size. For given $M \times N$ image patch and $p \times q$ annihilating filter, we now denote the associated spaces for the Hankel matrix as $\mathcal{H}(M, N; p, q)$. Then, for a given noisy image patch $\mathbf{M} \in \mathbb{R}^{M \times N}$ and $p \times q$ annihilating filter size, our impulse-noise removal algorithm can be implemented by solving the following sparse + low-rank decomposition under the

Hankel structure matrix constraint:

$$(P) \quad \min_{\mathbf{L,S}} \quad \|\mathbf{L}\|_* + \tau\|\mathbf{S}\|_1 \quad (11)$$
$$\text{subject to} \quad \mathbf{L} + \mathbf{S} = \mathscr{H}(\mathbf{M}),$$
$$\mathbf{L,S} \in \mathcal{H}(M, N; p, q)$$

Given that the sparse components in image patch are also sparse in a lifted Hankel structure, $(P)$ can be further simplified to

$$(P') \quad \min_{\mathbf{X,E}} \quad \|\mathscr{H}(\mathbf{X})\|_* + \tau\|\mathbf{E}\|_1$$
$$\text{subject to} \quad \mathbf{X} + \mathbf{E} = \mathbf{M}.$$

where, with some slight abuse of notation, $\tau$ denotes an appropriately scaled version from $\tau$ in $(P)$. Note that $\mathbf{E}$ is now in the image patch domain, unlike $\mathbf{S}$ in the lifted Hankel matrix structured matrix domain in $(P)$. The advantage of $(P')$ over $(P)$ is an associated simpler optimization method. More specifically, if we apply a factorized form of nuclear norm relaxation, then the final problem formulation of the optimization problem can then be expressed as

$$\min_{\mathbf{E,X},\{(\mathbf{U,V})|\mathbf{UV}^H = \mathscr{H}(\mathbf{X})\}} \quad \|\mathbf{U}\|_F^2 + \|\mathbf{V}\|_F^2 + \tau\|\mathbf{E}\|_1$$
$$(12)$$
$$\text{subject to} \quad \mathbf{X} + \mathbf{E} = \mathbf{M}. \quad (13)$$

The constraints in (12) and (13) can be handled using the alternating direction method of multiplier (ADMM) [30], [37]. The associated Lagrangian function ADMM is given by:

Then, each sub-problem is simply obtained from (14). More specifically, we have

$$\mathbf{E}^{(k+1)} = \arg\min_{\mathbf{E}} \tau\|\mathbf{E}\|_1 + \frac{\beta}{2}\|\mathbf{X}^{(k)} + \mathbf{E} - \mathbf{M} + \mathbf{\Theta}^{(k)}\|_F^2$$
$$(15)$$

$$\mathbf{X}^{(k+1)} = \arg\min_{\mathbf{X}} \frac{\beta}{2}\|\mathbf{X} + \mathbf{E}^{(k+1)} - \mathbf{M} + \mathbf{\Theta}^{(k)}\|_F^2$$
$$+ \frac{\mu}{2}\|\mathscr{H}(\mathbf{X}) - \mathbf{U}^{(k)}\mathbf{V}^{(k)H} + \mathbf{\Lambda}^{(k)}\|_F^2 \quad (16)$$

$$\mathbf{U}^{(k+1)} = \arg\min_{\mathbf{U}} \frac{1}{2}\|\mathbf{U}\|_F^2$$
$$+ \frac{\mu}{2}\|\mathscr{H}(\mathbf{X}^{(k+1)}) - \mathbf{U}\mathbf{V}^{(k)H} + \mathbf{\Lambda}^{(k)}\|_F^2 \quad (17)$$

$$\mathbf{V}^{(k+1)} = \arg\min_{\mathbf{V}} \frac{1}{2}\|\mathbf{V}\|_F^2$$
$$+ \frac{\mu}{2}\|\mathscr{H}(\mathbf{X}^{(k+1)}) - \mathbf{U}^{(k+1)}\mathbf{V}^H + \mathbf{\Lambda}^{(k)}\|_F^2 \quad (18)$$

$$\mathbf{\Theta}^{(k+1)} = \mathbf{X}^{(k+1)} + \mathbf{E}^{(k+1)} - \mathbf{M} + \mathbf{\Theta}^{(k)} \quad (19)$$

$$\mathbf{\Lambda}^{(k+1)} = \mathscr{H}(\mathbf{X}^{(k+1)}) - \mathbf{U}^{(k+1)}\mathbf{V}^{(k+1)H} + \mathbf{\Lambda}^{(k)} \quad (20)$$

It is easy to show that the first step can be simply reduced to a single instance of soft-thresholding in the image patch domain rather than in a lifted Hankel matrix space

$$\mathbf{E}^{(k+1)} = \mathcal{S}_{\tau/\beta}\left(\mathbf{M} - \mathbf{X}^{(k)} - \mathbf{\Theta}^{(k)}\right), \quad (21)$$

where $\mathcal{S}_\tau$ denotes the pixel-by-pixel soft-thresholding approach with a threshold value of $\tau$. The soft-thresholding operation is described as $\mathcal{S}_\tau(\mathbf{x}) = \max\{0, |x_i| - \tau\}\text{sgn}(x_i)$. The simple thresholding step in (21) is the main motivation behind why we prefer $(P')$ over $(P)$. At this point, the second step becomes

$$\mathbf{X}^{(k+1)} = \frac{1}{\mu + \beta}\left(\mu\mathscr{H}^\dagger\left\{\mathbf{U}^{(k)}\mathbf{V}^{(k)H} - \mathbf{\Lambda}^{(k)}\right\}\right.$$
$$\left. - \beta\left(\mathbf{E}^{(k+1)} - \mathbf{M} + \mathbf{\Theta}^{(k)}\right)\right), \quad (22)$$

where $\mathscr{H}^\dagger$ corresponds to the Penrose-Moore pseudo-inverse mapping from our block Hankel structure to a patch, which is calculated as follows:

$$\mathscr{H}^\dagger = \left(\mathscr{H}^H\mathscr{H}\right)^{-1}\mathscr{H}^H . \quad (23)$$

Note that the adjoint operator $\mathscr{H}^H(\mathbf{A})$ adds multiple elements of $\mathbf{A}$ and put it back to the patch coordinate, while $\left(\mathscr{H}^H\mathscr{H}\right)^{-1}$ denotes the division by the number of multiple correspondences. Hence, the role of the pseudo-inverse is to take the average value and put it back to the patch coordinate. For more details on this step, see Appendix B in Supplementary Material.

Next, the sub-problems for $\mathbf{U}$ and $\mathbf{V}$ can be easily calculated by taking the derivative with respect to each matrix. For example, the derivative of cost function for

$$L(\mathbf{U,V,E,X,\Theta,\Lambda}) := \frac{1}{2}\left(\|\mathbf{U}\|_F^2 + \|\mathbf{V}\|_F^2\right) + \tau\|\mathbf{E}\|_1$$
$$+ \frac{\beta}{2}\|\mathbf{X} + \mathbf{E} - \mathbf{M} + \mathbf{\Theta}\|_F^2 + \frac{\mu}{2}\|\mathscr{H}(\mathbf{X}) - \mathbf{UV}^H + \mathbf{\Lambda}\|_F^2 \quad (14)$$

$\mathbf{U}$ is given by

$$
\begin{aligned}
\frac{\partial L}{\partial \mathbf{U}} &= \frac{\partial}{\partial \mathbf{U}} \left( \frac{1}{2} \|\mathbf{U}\|_F^2 + \frac{\mu}{2} \|\mathscr{H}(\mathbf{X}) - \mathbf{U}\mathbf{V}^H + \mathbf{\Lambda}\|_F^2 \right) \\
&= \mathbf{U} - \mu \left( \mathscr{H}(\mathbf{X}) - \mathbf{U}\mathbf{V}^H + \mathbf{\Lambda} \right) \mathbf{V} \\
&= \mathbf{U} \left( I + \mu \mathbf{V}^H \mathbf{V} \right) - \mu \left( \mathscr{H}(\mathbf{X}) + \mathbf{\Lambda} \right) \mathbf{V},
\end{aligned}
$$

and the closed-form solution of the sub-problem for $\mathbf{U}$ is obtained by setting $\partial L / \partial \mathbf{U} = \mathbf{0}$. In the similar way, the derivative with respect to $\mathbf{V}$ can be obtained. Accordingly, the closed-form update equations for $\mathbf{U}$ and $\mathbf{V}$ are given by

$$
\begin{aligned}
\mathbf{U}^{(k+1)} &= \mu \left( \mathscr{H}(\mathbf{X}^{(k+1)}) + \mathbf{\Lambda}^{(k)} \right) \mathbf{V}^{(k)} \\
&\quad \left( I + \mu \mathbf{V}^{(k)H} \mathbf{V}^{(k)} \right)^{-1}, \qquad (24)
\end{aligned}
$$

$$
\begin{aligned}
\mathbf{V}^{(k+1)} &= \mu \left( \mathscr{H}(\mathbf{X}^{(k+1)}) + \mathbf{\Lambda}^{(k)} \right)^H \mathbf{U}^{(k+1)} \\
&\quad \left( I + \mu \mathbf{U}^{(k+1)H} \mathbf{U}^{(k+1)} \right)^{-1}. \qquad (25)
\end{aligned}
$$

Although the original Hankel matrix $\mathscr{H}(\mathbf{X})$ has large dimensions, it is important to note that our algorithm using (24) and (25) only requires the matrix inversion of $r \times r$ matrices, where $r$ denotes the estimated rank of the Hankel matrix from LMaFit [31]. This significantly reduces the overall computational complexity.

Specifically, before we apply ADMM (in Eq. (15)-(22)), the initial estimate $\mathbf{U}$ and $\mathbf{V}$ must be determined with an estimated rank. To do this, we employed an SVD-free algorithm known as the row-rank factorization model (LMaFit) [31]. More specifically, for a low-rank matrix $\mathbf{Z}$, LMaFit solves the following optimization problem (see [31, Eq.(1.4)])

$$
\min_{\mathbf{U},\mathbf{V},\mathbf{Z}} \frac{1}{2} \|\mathbf{U}\mathbf{V}^H - \mathbf{Z}\|_F^2
$$

$$
\text{subject to} \quad \mathbf{Z}_{i,j} = \left( \mathscr{H}(\mathbf{M}) \right)_{i,j}, \quad (i,j) \in \Omega, \qquad (26)
$$

where $\Omega$ denotes the sampled indices. Because the impulse-noise locations are not known a priori, when applying LMaFit, we set $\Omega$ to represent all pixel locations, as in this LMaFit step we are only interested in finding the initial estimates of $\mathbf{U}$ and $\mathbf{V}$ which actually give the estimated rank, $r$. The unknown location of $\Omega$ is then implicitly identified as the complement set of the support of estimated sparse outliers in our ADMM step in (21).

There is one potential drawback of the low-rank factorization model (26), as the non-convexity of the optimization problem may prevent one from obtaining a global solution. Moreover, the approach requires an initial rank estimate. In LMaFit [31], the authors presented convincing evidence to show that (a) on a wide range of

problems tested, the low-rank factorization model (26) is empirically reliable and (b) the initial rank estimate does not need to be close to the exact rank. Specifically, LMaFit solves a linear equation with respect to $\mathbf{U}$ and $\mathbf{V}$ to find their updates and relaxes the updates by taking the average between the previous iterations. Moreover, the rank update step can be done automatically by detecting abrupt changes of the diagonal elements of QR factorization [31]. Although the problem (26) is a non-convex case due to the multiplication of $\mathbf{U}$ and $\mathbf{V}$, the convergence of LMaFit to a stationary point was analyzed in detail [31]. Moreover, another important breakthrough in this field is the recent work by Zhu et al [38], which rigorously show that the all local minimizers of LMaFit type matrix factorization approaches are saddle points such that any iterative method converges to a global minimizer. Thus, our initialization with LMaFit is assumed to be a good estimate of $\mathbf{U}$ and $\mathbf{V}$. However, LMaFit alone cannot recover the block Hankel structure which explains the reason we use ADMM later to impose the structure.

## IV. Extension to Multichannel Impulse-Noise Removal

In many applications, images are obtained through multiple measurement channels. For example, in a colour image, multiple images are measured throughout R (red), G (green) and B (blue) detectors. In multispectral imaging for remote sensing applications, a scene is measured through many spectral bands. In these applications, the underlying structure is identical such that there are strong correlations between different channel measurements. Regarding random impulse-noise contamination for multichannel measurements, we may encounter two different scenarios. First, noisy pixel locations can be independent between the channels, Second, noisy pixel locations can be identical across the channels. The first scenario is commonly observed when independent detectors are used for each channel. On the other hand, when a spectrometer is used to split an input into multiple channels, noisy pixel locations may be common across the channel. Therefore, in this section, we are interested in extending single-channel robust ALOHA to address these two cases.

### A. Multichannel Image Modeling

Let $f(\mathbf{r})$ denote an underlying image patch that is common for all channel measurements, and $\hat{f}(\boldsymbol{\omega})$ be its spectrum. Then, as shown in Fig. 4(a), the spectrum of the $i$-th channel measurement can be modeled as follows:

$$
\hat{x}_i(\boldsymbol{\omega}) = \hat{s}_i(\boldsymbol{\omega}) \hat{f}(\boldsymbol{\omega}), \quad i = 1, \cdots, C. \qquad (27)
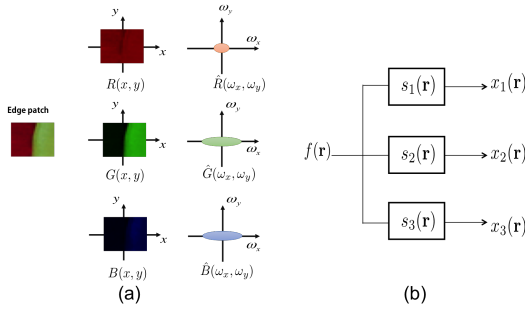$$

Fig. 4. (a) Spectral distribution across channels. (b) Multichannel measurement model.

Here, $\hat{s}_i(\omega)$ denotes a spectral modulation function of the $i$-th channel, and $C$ refers to the number of channels. The model (27) assumes that each channel measurement retains the textures of the underlying images by means of channel specific modulation, the properties of which were extensively exploited in multichannel deconvolution problems [39], as illustrated in Fig. 4(b). Accordingly, it is easy to derive the following *inter-channel annihilating filter relation*

$$s_j(\mathbf{r}) * x_i(\mathbf{r}) - s_i(\mathbf{r}) * x_j(\mathbf{r}) = 0, \quad \forall \mathbf{r}, \quad i \neq j, \quad (28)$$

which was also a key property in these multichannel deconvolution algorithms [39].

To exploit the inter-channel annihilating property in our robust ALOHA, we follow the standard trick of [39] to construct the following matrix

$$\mathcal{Y} = [\mathscr{H}(\mathbf{X}_1) \ \mathscr{H}(\mathbf{X}_2) \ \cdots \ \mathscr{H}(\mathbf{X}_C)] . \quad (29)$$

In this matrix, $\mathscr{H}(\mathbf{X}_i)$ denotes the Hankel structured matrix constructed from the $i$-th channel measurement $x_i(\mathbf{r})$. Then, the authors in [39] showed that

$$\mathcal{Y}\mathcal{S}_1 = \mathbf{0},$$

where $\mathcal{S}_1$ is defined recursively, as follows

$$\mathcal{S}_{C-1} \triangleq \begin{bmatrix} \bar{\mathbf{s}}_C \\ -\bar{\mathbf{s}}_{C-1} \end{bmatrix} \quad (30)$$

$$\mathcal{S}_t \triangleq \begin{bmatrix} \bar{\mathbf{s}}_{t+1} & \bar{\mathbf{s}}_{t+2} & \cdots & \bar{\mathbf{s}}_C & \mathbf{0} \\ -\bar{\mathbf{s}}_t & & & & \\ & -\bar{\mathbf{s}}_t & & & \mathcal{S}_{t+1} \\ & & \ddots & & \\ & & & -\bar{\mathbf{s}}_t & \end{bmatrix}, \quad (31)$$

and $\bar{\mathbf{s}}_i := \overline{\mathrm{VEC}(\mathbf{S}_i)}$ denotes the reverse-ordered, vectorized spectral modulation filter for the $i$-th channel. The main idea behind the recursive relationship is to consider all combinations of $i \neq j$ of (28) from $C$-channels [39].

Because $\dim \mathrm{NUL}(\mathcal{Y}) = \mathrm{rank}(\mathcal{S}_1) = \binom{C}{2} =$

$C(C-1)/2$, we have

$$\mathrm{rank} \ \mathcal{Y} \ \leq \ rC - \frac{C(C-1)}{2} = \frac{C(2r - C + 1)}{2}, \quad (32)$$

when $r$ denotes the maximum rank of $\mathscr{H}(\mathbf{X}_i), i = 1, \cdots, C$. Hence, by setting the annihilating filter size such that it is sufficiently large, we can sure that $\mathcal{Y}$ has a row rank, after which the aforementioned sparse+ low-rank decomposition approach can be used for impulse-noise removal.

### B. Optimization Methods

*1) Channel-independent impulse-noise:* When the locations of the impulse noise are independent between channels, then the associated optimization problem is very similar to that of the single-channel problem. More specifically, with some slight abuse of the notation, if we define

$$\mathbf{M} = [\mathbf{M}_1 \ \cdots \ \mathbf{M}_C], \ \mathbf{X} = [\mathbf{X}_1 \ \cdots \ \mathbf{X}_C], \ \mathbf{E} = [\mathbf{E}_1 \ \cdots \ \mathbf{E}_C], \quad (33)$$

such that the each channel measurement is given by

$$\mathbf{M}_i = \mathbf{X}_i + \mathbf{E}_i,$$

the optimization problem then becomes

$$\min_{\mathbf{E}, \{(\mathbf{U}, \mathbf{V}) | \mathbf{U}\mathbf{V}^H = \mathscr{H}(\mathbf{X})\}} \quad \|\mathbf{U}\|_F^2 + \|\mathbf{V}\|_F^2 + \tau \|\mathbf{E}\|_1 \quad (34)$$

$$\text{subject to} \quad \mathscr{H}(\mathbf{X}) = [\mathscr{H}(\mathbf{X}_1) \ \mathscr{H}(\mathbf{X}_2) \ \cdots \ \mathscr{H}(\mathbf{X}_C)]$$
$$\mathbf{X} + \mathbf{E} = \mathbf{M} . \quad (35)$$

In this case, the Lagrangian cost function and the associated subproblems are identical to Eqs. (14) and (16)-(22), respectively.

*2) Common impulse-noise locations:* When the noisy pixel locations are common across channels, we need a non-trivial algorithmic modification that comes by using a common sparsity inducing matrix norm penalty. More specifically, a common support condition of sparse components $\mathbf{E}$ should be imposed across the channels. In this paper, this constraint is formulated using the group-wise mixed $l_{1,2}$ norm

$$\mathbf{E} = [\mathbf{E}_1 \ \cdots \ \mathbf{E}_C] \quad \Longrightarrow \quad \|\mathbf{E}\|_{1,2} := \sum_{i,j} \sqrt{\sum_{k=1}^{C} \mathbf{E}_k(i,j)^2} \quad (36)$$

Accordingly, Eq. (14) can be converted to

$$L(\mathbf{U}, \mathbf{V}, \mathbf{E}, \mathbf{X}, \mathbf{\Theta}, \mathbf{\Lambda}) :=$$

$$\frac{1}{2}\left(\|\mathbf{U}\|_F^2 + \|\mathbf{V}\|_F^2\right) + \tau\|\mathbf{E}\|_{1,2} + \frac{\beta}{2}\|\mathbf{X} + \mathbf{E} - \mathbf{M} + \mathbf{\Theta}\|_F^2$$

$$+ \frac{\mu}{2}\|\mathscr{H}(\mathbf{X}) - \mathbf{U}\mathbf{V}^H + \mathbf{\Lambda}\|_F^2. \quad (37)$$

Then, instead of using (15), the corresponding sub-problem for $\mathbf{E}$ has the following closed-form solution [40]:

$$\mathbf{E}^{(k+1)} \;=\; \mathcal{S}^{ch}_{\tau/\beta}\left(\mathbf{M} - \mathbf{X}^{(k)} - \mathbf{\Theta}^{(k)}\right) \qquad (38)$$

where, for $\mathbf{E}$ in (36), $\mathcal{S}^{ch}_{\lambda}(\mathbf{E})$ is defined as

$$\mathcal{S}^{ch}_{\lambda}(\mathbf{E}) := \left[\mathcal{S}^{vec}_{\lambda}(\mathbf{E}_1) \cdots \mathcal{S}^{vec}_{\lambda}(\mathbf{E}_C)\right]$$

and

$$\left[\mathcal{S}^{vec}_{\lambda}(\mathbf{E}_k)\right]_{ij} = \frac{\mathbf{E}_k(i,j)}{\sqrt{\sum_{k=1}^{C}|\mathbf{E}_k(i,j)|^2}}$$
$$\times \max\left\{\sqrt{\sum_{k=1}^{C}|\mathbf{E}_k(i,j)|^2} - \lambda, 0\right\}(39)$$

Other remaining sub-problems are mainly similar to those expressed by (16)-(22).

## V. Experimental Results

### A. Removal of Random-valued Impulse Noise (RVIN)

We first performed denoising experiments using randomly distributed random-valued impulse-noise (RVIN) that corrupts 25% and 40% of all image pixels. The RVIN is generated as follows. Let $x_{ij} := \mathbf{X}(i,j)$ and $N(x_{ij})$ be the original pixel value at location $(i,j)$ and the contaminated pixel with impulse noise at location $(i,j)$, respectively. When the dynamic range of the pixel value is given as $[d_{min}\ d_{max}]$, RVIN is described as

$$N(x_{ij}) = \begin{cases} d_{ij} & \text{with probability } p \\ x_{ij} & \text{with probability } 1-p \end{cases} \qquad (40)$$

where $d_{ij}$ is a random number within the range of $[d_{min}\ d_{max}]$ established by the uniform random probability density function, and $p$ is the proportion of noisy pixels with respect to all pixels.

The test sets consisted of the Baboon, Barbara, Boat, Cameraman, House, Lena and Peppers images. All test images were rescaled to have values between 0 and 1. For comparison, a median filter method (MATLAB built-in function 'medfilt2', indicated as MF in the figures) was used as the simplest reference algorithm, and the existing algorithms such as ACWMF [3], a locally low-rank analysis using alternating least squares (k-ALS) [28], wavelet frame-based blind inpainting (wavelet) [29], and TVL1 [41] were also used. In particular, the k-ALS algorithm is a learning-based algorithm that obtains its results from a non-convex robust low-rank formulation of patches using an initialized learned dictionary [44]; therefore, k-ALS is a good reference algorithm to use when investigating the fundamental differences

between Hankel-based and image-based sparse and low-rank approaches. On the other hand, wavelet frame-based blind inpainting [29] exploits the sparsity in the wavelet domain with the estimation of sparse outliers. In addition, a state-of-the-art compressed sensing based sparse recovery approach [42] (henceforth denoted as 'Blind') was compared, which is distinct from the total variational inducing sparsity [41]. The non-local sparse PCA method (NLSPCA) [43] is another a state-of-the-art learning-based approach for noise removal which combines elements of dictionary learning and sparse patch-based representations of images. While the original NLSPCA was developed for Poisson noise removal, the noise patterns often appear to be similar to impulse-noise, especially in environments with low photon counts. Therefore, the proposed algorithm was also compared with NLSPCA. The original codes from the original authors were used, and the parameters for the these algorithms were optimized to result in the best performance levels.
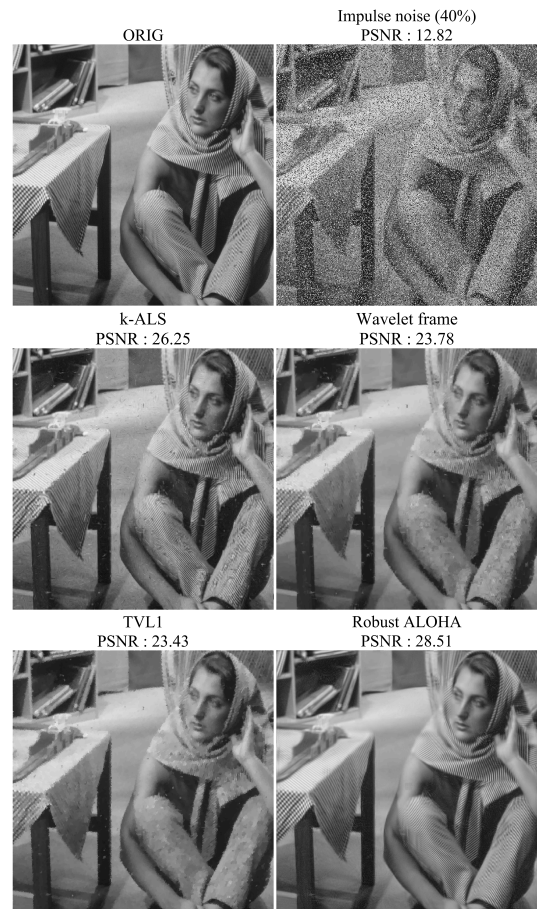


Fig. 5. Reconstructed Barbara images by various methods from 40% random valued impulse noise.

The parameters for the proposed method are given in Table I. The maximum iteration number of ADMM

TABLE I
HYPER-PARAMETERS USED IN THE PROPOSED ALGORITHM. $\mu$ AND $\beta$ OF ADMM ARE 1. FOR LMaFit, INITIAL RANK WITH
INCREASING STRATEGY IS ONE AND TOLERANCES FOR 25%(40%) IMPULSE NOISE IS 0.2(0.3).

|  | Baboon $(512 \times 512)$ | Barbara $(512 \times 512)$ | Boat $(512 \times 512)$ | Cameraman $(256 \times 256)$ | House $(256 \times 256)$ | Lena $(512 \times 512)$ | Peppers $(255 \times 255)$ |
|---|---|---|---|---|---|---|---|
| Size of $\mathbf{X}$ | $45 \times 45$ | $25 \times 25$ | $25 \times 25$ | $31 \times 31$ | $25 \times 25$ $(45 \times 45)$ | $25 \times 25$ | $25 \times 25$ $(45 \times 45)$ |
| Size of $\mathbf{H}$ | $13 \times 13$ | $11 \times 11$ | $11 \times 11$ | $13 \times 13$ | $11 \times 11$ $(13 \times 13)$ | $11 \times 11$ | $9 \times 9$ $(13 \times 13)$ |
| Size of $\mathscr{H}(\mathbf{X})$ | $1089 \times 169$ | $225 \times 121$ | $225 \times 121$ | $361 \times 169$ | $225 \times 121$ $(1089 \times 169)$ | $225 \times 121$ | $289 \times 81$ $(1089 \times 169)$ |
| $\tau(\times 10^{-2})$ | 10 (7.5) | 10 | 10 | 10 (7.5) | 10 (7.5) | 10 | 10 (7.5) |

TABLE II
RECONSTRUCTION TIME OF OTHER ALGORITHMS FROM 25% AND 40% RANDOM VALUED IMPULSE NOISE (RVIN).

| Test Images | Algorithms | MF | ACWMF | k-ALS [28] | Wavelet [29] | TVL1 [41] | Blind [42] | NLSPCA [43] | Proposed |
|---|---|---|---|---|---|---|---|---|---|
| Baboon | 25% | 0.027 | 1.1 | 71 | 197 | 2.12 | 0.94 | 357.5 | 745.94 |
| (512x512) | 40% | 0.026 | 1.0 | 71.15 | 197 | 2.16 | 1.01 | 352.9 | 495.77 |
| Cameraman | 25% | 0.01 | 0.26 | 19.22 | 43.19 | 0.26 | 0.20 | 111.1 | 370.49 |
| (256x256) | 40% | 0.01 | 0.26 | 19.5 | 42.71 | 0.26 | 0.33 | 92.2 | 277.8 |

TABLE III
RECONSTRUCTION IMAGE PSNR BY VARIOUS DENOISING ALGORITHMS FROM 25% AND 40% RANDOM VALUED IMPULSE NOISE
(RVIN). THE HIGHEST PSNR IN EACH IMAGE ARE HIGHLIGHTED WITH BOLDFACE.

| Test Images | Algorithms | Noisy | MF | ACWMF | k-ALS [28] | Wavelet [29] | TVL1 [41] | Blind [42] | NLSPCA [43] | Proposed |
|---|---|---|---|---|---|---|---|---|---|---|
| Baboon | 25% | 15.53 | 22.01 | 23.14 | 23.37 | 23.91 | 23.39 | 20.44 | 19.06 | **24.85** |
|  | 40% | 13.52 | 20.52 | 21 | 22.02 | 22.01 | 21.68 | 20.17 | 18.37 | **22.48** |
| Barbara | 25% | 14.84 | 23.62 | 24.59 | 29.15 | 26.29 | 24.99 | 22.85 | 20.02 | **33.26** |
|  | 40% | 12.82 | 21.14 | 22.86 | 26.25 | 23.78 | 23.43 | 22.29 | 18.37 | **28.69** |
| Boat | 25% | 15.37 | 27.27 | 28.09 | 29.65 | 29.81 | 28.64 | 24.21 | 21.03 | **30.64** |
|  | 40% | 13.31 | 23.52 | 25.73 | **27.14** | 26.75 | 26.19 | 23.56 | 19.56 | 26.96 |
| Cameraman | 25% | 14.44 | 24.28 | 24.69 | 25.55 | 26.37 | 25.58 | 20.67 | 19.21 | **26.81** |
|  | 40% | 12.37 | 20.61 | 22.13 | 23.11 | 23.15 | 23 | 20.15 | 17.36 | **23.4** |
| House | 25% | 15.31 | 29.08 | 29.74 | 33.19 | 32.78 | 31.16 | 25.56 | 22.28 | **34.45** |
|  | 40% | 13.27 | 24.36 | 27.44 | 29.91 | 29.12 | 28.07 | 24.25 | 20.23 | **29.97** |
| Lena | 25% | 15.29 | 30.07 | 30.75 | 33.07 | 32.89 | 31.9 | 26.75 | 22.45 | **34.44** |
|  | 40% | 13.23 | 24.6 | 28.78 | **30.84** | 29.58 | 29.14 | 25.74 | 20.13 | 30.6 |
| Peppers | 25% | 14.99 | 27.47 | 27.91 | 29.1 | 29.28 | 29.09 | 23.37 | 20.08 | **29.53** |
|  | 40% | 12.96 | 23.15 | 25.66 | **26.53** | 26.19 | 26.07 | 22.30 | 18.47 | 26.3 |

in Eq. (14) was set to 50, and the stopping criteria were defined as in earlier work [31] with the tolerance set to $10^{-4}$. For a quantitative evaluation, we used the PSNR (peak signal-to-noise ratio). Specifically, when the reference signal ($\mathbf{y}$) is given, the PSNR of the reconstructed image ($\mathbf{x}$) is calculated as follows:

$$\text{PSNR}(\mathbf{x}) = 20 \log_{10} \left( \frac{\|\mathbf{y}\|_\infty}{1/\sqrt{N} \times \|\mathbf{y} - \mathbf{x}\|_2} \right).$$

For rapid implementation, we used a TITAN GTX graphics card as a graphics processor unit (GPU) and an i7-4770k CPU. The codes were written in MATLAB (Mathworks, Natick) using the GPU library. To accelerate the algorithm, most parts of the MATLAB codes were implemented using the Compute Unified Device Architecture (CUDA) for GPUs. However, the LMaFit routine, which is one of the computational bottlenecks, was not parallelized because we used the original implementation by the authors. The computation times for various algorithms for the Baboon and Cameraman images at 25% and 40% RVIN are listed in Table II. Due to the low-rank matrix completion, the proposed method is computationally most expensive, which is the main limitation of the current implementation.
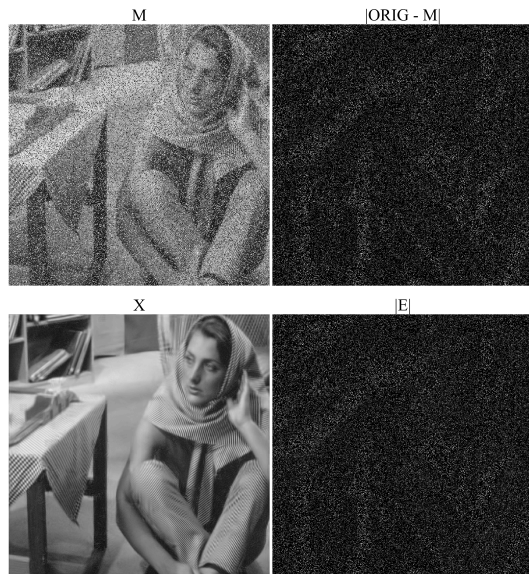
Fig. 6. **M**: the measured noisy image. |ORIG – **M**|: the residual image between noisy image (**M**) and original image (ORIG). **X**: the decomposed low-rank part, and **E**: the decomposed sparse component. Here, $|\cdot|$ is the element-by-element operator that takes the absolute value.

However, the performance improvement is quite noticeable. We summarized the PSNR results in Table III for all reconstructed images. We observed that the proposed method provides much better or well-matched results compared to the existing state-of-the-art methods. In particular, our method significantly outperformed for images having complex texture patterns (such as the Barbara image with 5dB improvement) in terms of the visual and quantitative quality levels. In some cases, k-ALS showed better results than ours with 0.2dB improvement; however, the differences are fairly negligible. Fig. 5 shows the typical reconstruction result, presenting a noticeable enhancement by robust ALOHA in terms of both visual quality and quantitative measures. In order to show that the proposed sparse + low-rank decomposition approach properly decomposes the impulse noise from the images, the decomposed sparse + low-rank components are illustrated in Fig. 6. This figure indicates that the sparse component (|**E**|) appears similar to the additive impulse noise, as indicated by |ORIG – **M**|, where ORG denotes an original image and $|\cdot|$ is the element-by-element operator that takes the absolute value.

Among the various conventional methods, k-ALS was the best, so we performed additional study with various noise percentage. Table IV shows that for the case of the highly textured images such as Barbara, the proposed method outperformed k-ALS for most of the noise contamination level. Even for smooth images such as Lena, the proposed method was better than k-ALS at moderate

noise contamination. Again, the main weakness of the proposed method is the computational time as shown in Table V for two different size of images.

TABLE IV
RECONSTRUCTION IMAGE PSNR BY ROBUST ALOHA AND k-ALS ALONG WITH VARIOUS DENSITY OF RANDOM VALUED IMPULSE NOISE (RVIN).

| Test Images | noise density | 10% | 25% | 50% | 75% | 90% |
|---|---|---|---|---|---|---|
| Barbara | k-ALS | 31.35 | 29.13 | 23.22 | 17.16 | **13.94** |
| | Proposed | **38.53** | **33.32** | **25.02** | **17.39** | 13.74 |
| Lena | k-ALS | 35.69 | 33.27 | **28.29** | **19.07** | **15.24** |
| | Proposed | **38.91** | **34.25** | 27.14 | 19.01 | 14.36 |

TABLE V
RECONSTRUCTION TIME (S) OF K-ALS AND ROBUST ALOHA ALONG WITH VARIOUS DENSITY OF RANDOM VALUED IMPULSE NOISE (RVIN).

| Test Images | noise density | 10% | 25% | 50% | 75% | 90% |
|---|---|---|---|---|---|---|
| Baboon | k-ALS | 76.69 | 75.35 | 72.16 | 71.53 | 72.02 |
| (512x512) | Proposed | 959.09 | 725.97 | 581.05 | 377.64 | 155.98 |
| Cameraman | k-ALS | 21.41 | 21.05 | 20.21 | 19.67 | 19.83 |
| (256x256) | Proposed | 464.85 | 364.71 | 298.75 | 217.97 | 129.21 |

### B. Comparison with conventional RPCA

To verify that lifting to a Hankel matrix is beneficial for a performance improvement, we also applied the standard RPCA as an impulse-noise removal algorithm and compared the results. The reason we used RPCA as baseline comparison is that original RPCA [45] was proposed to reconstruct low-rank matrix even with sparse outlier, and this purpose aligns with our target problem in Eq. (9) and ($P$). Two types of RPCA were implemented: one using whole images, and the other using an image patch of the same size as our robust ALOHA. Note that the standard RPCA uses an image or patches as they are, without lifting them into a Hankel structured matrix. For RPCA, we used the software packages provided by the original authors in earlier work [46]. We chose the parameters for the best PSNR results in each reconstruction. As shown in Fig. 7, the two RPCA implementation methods could not decompose impulse noise out of mixed measurements, and the detailed image structures were distorted. Additionally, the local patch-based sparse and low-rank models (k-ALS) [28] were also compared, and the results appeared better than that by the conventional RPCA framework. However, noise artifacts and distortions in the regions denoted
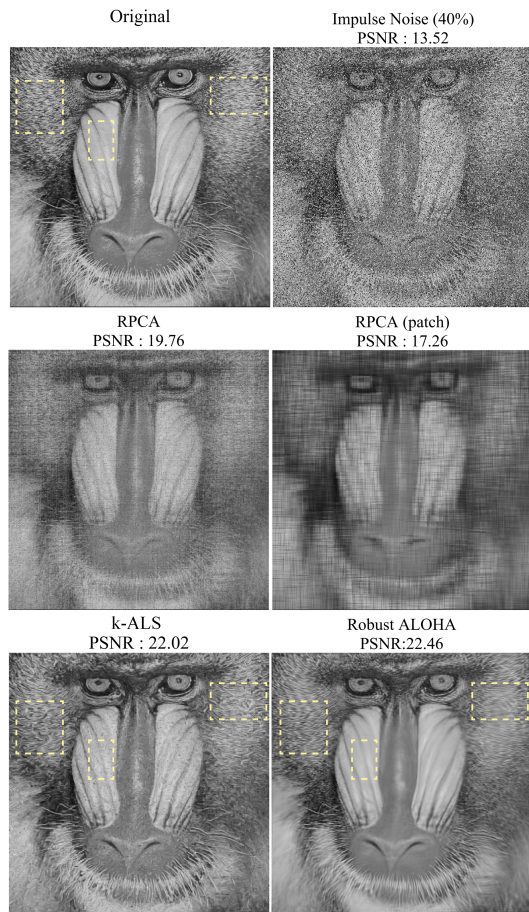
Fig. 7. Comparison with conventional RPCA approach with the proposed method under 40% random valued impulse noise. Boxed areas show the major differences between k-ALS and robust ALOHA.
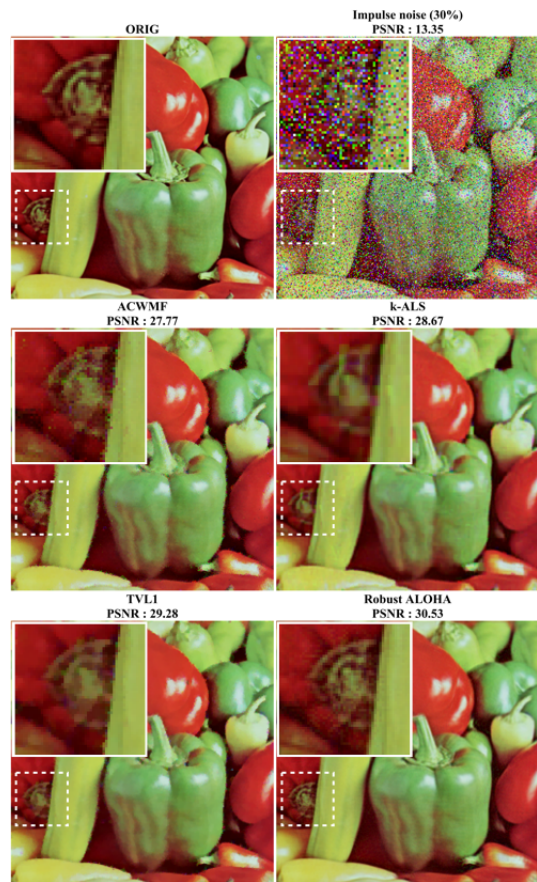


Fig. 8. Multichannel denoising results under 30% random valued impulse noise at the independent pixel locations at each RGB channels.

by yellows boxes were still noticeable. In particular, the reconstructed baboon hairs by k-ALS were highly distorted and the tissues around the noise in the k-ALS reconstruction contained severe noise. On the other hand, robust ALOHA provided nearly perfect noise removal. Such a remarkable performance improvement originated from image modeling which exploited the low-rankness of the annihilating filter-based Hankel matrix, which again confirms that the robust ALOHA is a superior image model and denoising algorithm for images corrupted with impulse noise.

## C. Multichannel Denoising

To verify that the proposed method can easily be extended to multichannel images, we conducted experiments with colour RGB images. As discussed earlier, the noisy pixel location can be either identical across channels or independent for each channel. Therefore, we conducted experiments under the two different scenarios. Fig. 8 shows the reconstruction result when 30% of

channel-independent impulse noise was added, whereas Fig. 9 corresponds to the scenario when 30% of impulse noise was added at the same locations across RGB channels. The proposed method provided more detailed structures (e.g. a bundle of peppers and the edges of the peppers) than the TVL1 reconstructions, as shown in Figs. 8-9. Moreover, the cartoon-like artifacts were significantly reduced in the proposed method. In the inset images, the detailed structures of the peppers are magnified to demonstrate the superior performance of the proposed method over other methods.

One of the interesting observations from these experiments was that the proposed reconstruction provided a better PSNR for the channel-independent impulse noise. This occurred because the noiseless pixel values from other channels could improve the image inpainting performance of noisy pixel values by exploiting the correlation between the channels.

## D. Algorithm convergence

Because reconstructions are based on patch-by-patch optimization, to verify the convergence of the algorithm,
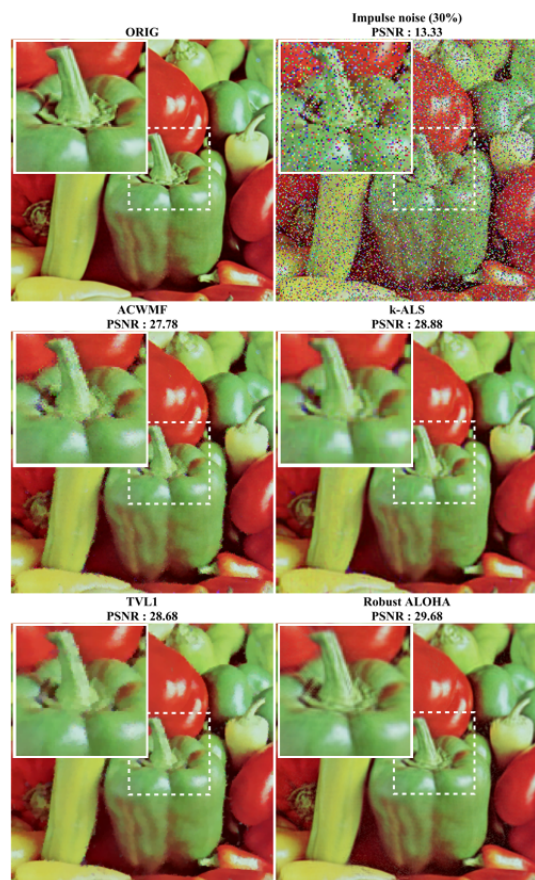
Fig. 9.   Multichannel denoising results under 30% random valued impulse noise at the common pixel locations across the RGB channels.

all of the patch data should be collected, and their convergence were analyzed. The Barbara image was used, and the corresponding convergence plot is illustrated in Fig. 10. Here, we calculated the NRMSE value for each patch per iteration. The total number of patches was 5184. In the box plot, the central mark (red line) is the median, and the edges of the box are the 25th and 75th percentiles, respectively. As observed in Fig. 10, the proposed algorithm converged as iteration process continues.
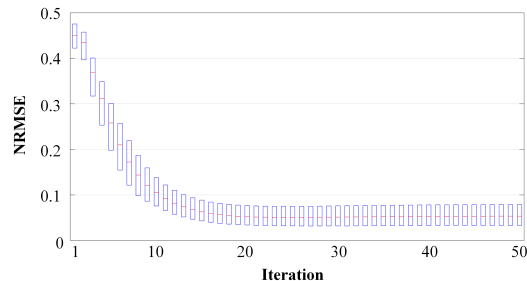


Fig. 10.   NRMSE graph along with ADMM iterations in Barbara image.

## VI. Discussion

### A. Spectral domain sparsity

Recall that the proposed robust ALOHA method was performed in a patch-by-patch manner without considering additional similar patches. This is an important difference compared to other denoising algorithms which use low-rank approaches [14], [47], [48]. While the authors in those studies [14], [47], [48] used patch-based low-rankness, all methods required additional redundancies from, for example, multiple dynamic frames [14], [47] or groups of similar spectral patches [48]. Although such additional redundant information may introduce a low-rankness condition, those approaches could not properly perform denoising without utilizing such additional redundancies. On the other hand, the robust ALOHA method exploits the low-rankness originating from the intrinsic spectral domain sparsity of an image patch. Therefore, no additional redundancy needs to be explored. Thus, we believe that robust ALOHA is more flexible and powerful.

Because the proposed robust ALOHA is based on the spectral domain sparsity, one may wonder that the formulation might be equivalent to imposing the sparsity directly in DFT domain for each patch. However, mathematically, this equivalent only holds when the locations of Diracs in the spectral domain is on a discrete grid and the Hankel matrix is constructed as a circulant matrix (see [18] for more details). However, in the proposed robust ALOHA, the spectral domain sparsity is imposed on a continuum based on the off-the-grid stream of Diracs model [18], which significantly improves the performance compared to the DFT domain sparsity implementation.

As briefly discussed in the introduction, a recent study [49] successfully demonstrated the accurate predictions of target locations under occlusion using the sparse + low-rank decomposition of a Hankel structured matrix. However, unlike our robust ALOHA, one-dimensional trajectories extracted from video sequences are required as inputs to construct the Hankel structured matrix, as the algorithm was derived based on the assumption that those trajectories follow linear time invariant state-space models, as has been suggested in [50]. On the other hand, the Hankel structured matrix in robust ALOHA stems from two-dimensional patches that exploit the spectral domain sparsity; thus, the construction of the Hankel matrix is different from that in earlier work [49]. Moreover, we exploit an SVD-free minimization algorithm [37] instead of the augmented Lagrangian method (ALM) in the aforementioned studies [49], [50] to reduce the computational burdens. Therefore, we believe that there

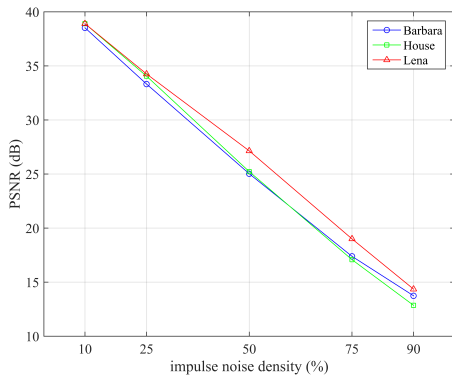are significant differences between the two approaches.



Fig. 11. Performance graph with respect to density of impulse noise.

### B. Modification for high noise contamination

As shown in Fig. 11, the performance degradation with the increasing impulse noise level was gradual. However, we found that the denoising performance beyond the noise density of 40 % did not provide significant gain over other algorithms. This was mainly due to the outlier detection step in (15), which results in a simple shrinkage operation for sparse outlier detection. Thus, by replacing $l_1$-based the outlier detection step in (15) with more sophisticated decision-based outlier detection algorithms [1], [4]–[7], we conjectured that that robust ALOHA may have significant improvement in performance especially at highly containimated impulse noise. To verify the conjecture, we performed simulations with salt-and-pepper noise at extremely high noise contamination. Recall that the salt-and-pepper noise is a special case of RVIN, as it has impulse noise with the intensity of the minimum and maximum values of the pixel dynamic range. Specifically, salt-and-pepper noise are given by

$$N(x_{ij}) = \begin{cases} d_{min} & \text{with probability } p/2 \\ d_{max} & \text{with probability } p/2 \\ x_{ij} & \text{with probability } 1-p \end{cases} \quad , \quad (41)$$

where the variables $p$, $d_{max}$, $d_{min}$ are defined in Eq. (40). This model was described as Noise Model 1 in [7] which demonstrated the significant performance gain of BDND based switching filter. Specifically, salt-and-pepper type impulse noise can be well detected by a decision-based outlier detection step such as adaptive median filter (AMF) or BNDN algorithm. Because the positions of the salt and noise locations are well detected by AMF, our robust ALOHA can accordingly be modified. More specifically, the sparse outliers estimation step is replaced by AMF, whereas the remaining steps in (16)-(20) are replaced by similar steps as in [17] to obtain the

low-rank components and the Lagrangian update. The pseudo-code implementation is given in Algorithm 2 in Appendix C in Supplementary Material.

Note that this modification is a heuristic modification of the algorithm assuming that the sparse outliers estimation step by AMF is sufficiently accurate. To demonstrate that our algorithm continues to outperform the existing algorithms, we compared our method with adaptive median filtering (AMF), and BDND based switching filter using 70% salt-and-pepper noise. The results in Fig. 12 clearly demonstrate that the proposed robust ALOHA outperforms all other algorithms.
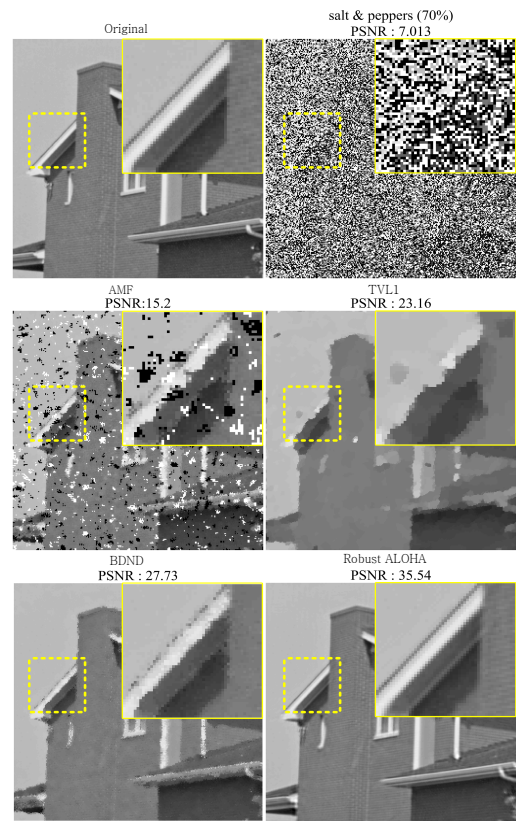


Fig. 12. Noise removal results using various methods under 70% salt-and-pepper noise. In Robust ALOHA, the sparse outlier detection step was replaced by an adaptive median filtering step, after which low-rank Hankel structured matrix completion was used to estimate the missing pixels in the sparse outlier locations.

Second, the switching based median filter [7] is well-known for its outstanding performance for extremely high impulse noise ratio. The switching median filter incorporated with a powerful impulse noise detection method, called the boundary discriminative noise detection (BDND). Once the corrupted pixel locations are identified by the BDND algorithm, a post-detection filtering was used to restore the original pixel values from the noisy pixels. Therefore, similar to the previous

experiment, we replaced our $l_1$-based outlier detection steps with the BDND step, after which the novel low-rank Hankel matrix completion is performed to estimate the uncorrupted pixels. The results in Fig. 13 clearly showed that at 80% of RVIN contamination under the same Noise Model 1 in [7], the proposed robust ALOHA significantly outperformed the switching based median filter.
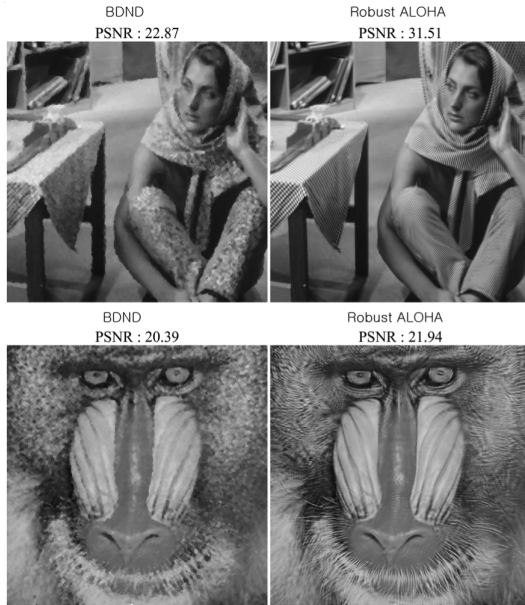


Fig. 13. Comparison of BDND switching median filter [7] and robust ALOHA at 80% salt-and-pepper noises.

### C. Potential extensions

Although robust ALOHA as reported here was derived based on the assumption that the spectrum of a noiseless image patch is sparse, the proposed algorithm can be extended for image patches which are sparse in other transform domains. To show this clearly, we assume that the underlying patch image is one-dimensional for simplicity, i.e., $\mathbf{x} \in \mathbb{R}^N$. In such a case, let the singular value decomposition of $\mathscr{H}(\mathbf{x})$ be given by $\mathscr{H}(\mathbf{x}) = \sum_{i=1}^r \sigma_i \mathbf{u}_i \mathbf{v}_i^H$, where $\mathbf{u}_i$ and $\mathbf{v}_i$ denote the $i$-th left and right singular vectors, respectively, with $\sigma_i$ as the associated singular values. Then, we have

$$\mathbf{x} = \mathscr{H}^\dagger \left( \sum_{i=1}^r \sigma_i \mathbf{u}_i \mathbf{v}_i^H \right) = \sum_{i=1}^r \sigma_i \mathscr{H}^\dagger \left( \mathbf{u}_i \mathbf{v}_i^H \right)$$
$$= \sum_{i=1}^r \lambda_i (\mathbf{u}_i * \bar{\mathbf{v}}_i^H) , \quad (42)$$

where $\lambda_i$ is equal to $\sigma_i$ divided by the number of multiple correspondences in the Hankel matrix, $\bar{\mathbf{v}}_i^H$ denotes the reverse-ordered vector $\mathbf{v}_i^H$, and the last equality follows

from the definition of the adjoint Hankel operation. A similar observation was recently made by Yin et al. [51]. In particular, they claimed that $\{\mathbf{u}_i\}$ corresponds to the local basis, whereas $\{\mathbf{v}_i\}$ denotes the non-local basis. Accordingly, they called the decomposition (42) the *convolution framelet* [51]. In ALOHA, the local basis $\mathbf{u}_i$ corresponds to the Fourier basis because we assume that the patch image is sparse in the Fourier domain, whereas the nonlocal basis, $\mathbf{v}_i$, are data-driven dictionaries. Thus, if an image patch is sparse in another transform domain, we can set $\mathbf{u}_i$ accordingly to make the decomposition (42) as concise as possible. The precise description of the algorithm and its theoretical justification may have significant potential, but providing this is beyond the scope of the present work.

### D. Patch Size

In principle, the patch size should be chosen so that the spectrum of a patch is sparse enough and it can be annihilated by a smaller size annihilating filter. In natural images, the spectral content of patches vary depending on the presence of complex textures, smooth backgrounds, etc. Moreover, the spectral components varies depending on locations within an image. Therefore, the optimal patch size should be chosen by trial and error. Empirically, we found that patch size between $25 \times 25$ and $45 \times 45$ worked well for most of test dataset. For best performance, our experience informs that for images with complicated textures such as Barboon, bigger patch size is usually better due to the high frequency spectral contents that needs to be annihilated with a large size annihilating filter. However, an automatic selection of optimal patch size is an important problem that needs to be further investigated in the future.

### VII. CONCLUSION

In this paper, we proposed the sparse + low-rank decomposition of annihilating filter-based Hankel matrices for impulse-noise removal. The new algorithm, called robust ALOHA, extends the conventional RPCA approaches by exploiting the spectral domain sparsity and the associated rank-deficient Hankel matrix. The robust ALOHA method was implemented using ADMM iteration with initialization using LMaFit algorithms. In our ADMM formulation, factorization-based nuclear norm minimization was used instead of SVD such that a computational gain was achieved. We demonstrated that robust ALOHA is either comparable to or capable of significantly outperforming state-of-the-art impulse-noise removal algorithms. Furthermore, we showed that robust ALOHA can be used for extremely high noisy

image by replacing the $l_1$-based sparse outlier detection step with a decision-based outlier detection algorithm. In addition, the extension to impulse-noise removal from color channels was very straightforward by concatenating the Hankel structure matrix in a side-by- side fashion and imposing low-rankness.

The superior performance of robust ALOHA clearly shows that an image modeling process using an annihilating-filter-based Hankel matrix is a very powerful tool with many image processing applications.

## ACKNOWLEDGMENT

## REFERENCES

[1] R. H. Chan, C.-W. Ho, and M. Nikolova, "Salt-and-pepper noise removal by median-type noise detectors and detail-preserving regularization," *IEEE Trans. Image Process.*, vol. 14, no. 10, pp. 1479–1485, 2005.

[2] H. Hwang, R. Haddad *et al.*, "Adaptive median filters: new algorithms and results," *IEEE Trans. Image Process.*, vol. 4, no. 4, pp. 499–502, 1995.

[3] T. Chen and H. R. Wu, "Adaptive impulse detection using center-weighted median filters," *IEEE Signal Process. Lett.*, vol. 8, no. 1, pp. 1–3, 2001.

[4] M. Yan, "Restoration of images corrupted by impulse noise and mixed gaussian impulse noise using blind inpainting," *SIAM Journal on Imaging Sciences*, vol. 6, no. 3, pp. 1227–1245, 2013.

[5] H.-L. Eng and K.-K. Ma, "Noise adaptive soft-switching median filter," *IEEE Trans. Image Process.*, vol. 10, no. 2, pp. 242–251, 2001.

[6] G. Pok, J.-C. Liu, and A. S. Nair, "Selective removal of impulse noise based on homogeneity level information," *IEEE Trans. Image Process.*, vol. 12, no. 1, pp. 85–92, 2003.

[7] P.-E. Ng and K.-K. Ma, "A switching median filter with boundary discriminative noise detection for extremely corrupted images," *IEEE Transactions on image processing*, vol. 15, no. 6, pp. 1506–1516, 2006.

[8] M. Nikolova, "A variational approach to remove outliers and impulse noise," *Journal of Mathematical Imaging and Vision*, vol. 20, no. 1-2, pp. 99–120, 2004.

[9] A. Chambolle and T. Pock, "A first-order primal-dual algorithm for convex problems with applications to imaging," *Journal of Mathematical Imaging and Vision*, vol. 40, no. 1, pp. 120–145, 2011.

[10] J. Yang, Y. Zhang, and W. Yin, "An efficient TVL1 algorithm for deblurring multichannel images corrupted by impulsive noise," *SIAM Journal on Scientific Computing*, vol. 31, no. 4, pp. 2842–2865, 2009.

[11] S. H. Chan, R. Khoshabeh, K. B. Gibson, P. E. Gill, and T. Q. Nguyen, "An augmented Lagrangian method for total variation video restoration," *IEEE Trans. Image Process.*, vol. 20, no. 11, pp. 3097–3111, 2011.

[12] R. E. Carrillo, K. E. Barner, and T. C. Aysal, "Robust sampling and reconstruction methods for sparse signals in the presence of impulsive noise," *IEEE Journal of Selected Topics in Signal Processing*, vol. 4, no. 2, pp. 392–408, 2010.

[13] A. Majumdar, N. Ansari, H. Aggarwal, and P. Biyani, "Impulse denoising for hyper-spectral images: A blind compressed sensing approach ," *Signal Processing*, vol. 119, pp. 136 – 141, 2016.

[14] H. Ji, C. Liu, Z. Shen, and Y. Xu, "Robust video denoising using low rank matrix completion," in *Proc. of IEEE Computer Soc. Conf. on Computer Vision and Pattern Recognition*. IEEE, 2010, pp. 1791–1798.

[15] Q. Ke and T. Kanade, "Robust $l_1$ norm factorization in the presence of outliers and missing data by alternative convex programming," in *IEEE Computer Society Conference on Computer Vision and Pattern Recognition, 2005. CVPR 2005.*, vol. 1. IEEE, 2005, pp. 739–746.

[16] P. P. Markopoulos, G. N. Karystinos, and D. A. Pados, "Optimal algorithms for $l_1$-subspace signal processing," *IEEE Transactions on Signal Processing*, vol. 62, no. 19, pp. 5046–5058, 2014.

[17] K. H. Jin and J. C. Ye, "Annihilating filter-based low-rank Hankel matrix approach for image inpainting," *IEEE Trans. Image Process.*, vol. 24, no. 11, pp. 3498–3511, Nov 2015.

[18] J. C. Ye, J. M. Kim, K. H. Jin, and K. Lee, "Compressive sampling using annihilating filter-based low-rank interpolation," *IEEE Trans. Inf. Theory*, vol. 63, no. 2, pp. 777–801, 2017.

[19] K. H. Jin, D. Lee, and J. C. Ye, "A general framework for compressed sensing and parallel mri using annihilating filter based low-rank hankel matrix," *IEEE Transactions on Computational Imaging*, vol. 2, no. 4, pp. 480–495, 2016.

[20] D. Lee, K. H. Jin, E. Y. Kim, S.-H. Park, and J. C. Ye, "Acceleration of MR parameter mapping using annihilating filter-based low rank Hankel matrix (ALOHA)," *Magn. Reson. Med.*, 5 JAN 2016, 10.1002/mrm.26081.

[21] J. Lee, K. H. Jin, and J. C. Ye, "Reference-free single-pass EPI Nyquist ghost correction using annihilating filter-based low rank Hankel structured matrix," *Magn. Reson. Med.*, 17 FEB 2016, 10.1002/mrm.26077.

[22] M. Vetterli, P. Marziliano, and T. Blu, "Sampling signals with finite rate of innovation," *IEEE Trans. Signal Process.*, vol. 50, no. 6, pp. 1417–1428, 2002.

[23] J. Min, L. Carlini, M. Unser, S. Manley, and J. C. Ye, "Fast live cell imaging at nanometer scale using annihilating filter based low rank Hankel matrix approach," in *Wavelets and Sparsity XVI, SPIE Optical Engineering + Applications*. International Society for Optics and Photonics, 2015, pp. 95 970V–95 970V.

[24] K. H. Jin, J. Min, and J. C. Ye, "Patch based low rank structured matrix completion for accelerated scanning microscopy," in *2015 IEEE 12th International Symposium on Biomedical Imaging (ISBI)*, April 2015, pp. 1236–1239.

[25] G. Ongie and M. Jacob, "Super-resolution MRI using finite rate of innovation curves," in *2015 IEEE 12th International Symposium on Biomedical Imaging (ISBI)*. IEEE, 2015, pp. 1248–1251.

[26] X. Qu, M. Mayzel, J.-F. Cai, Z. Chen, and V. Orekhov, "Accelerated NMR spectroscopy with low-rank reconstruction," *Angewandte Chemie International Edition*, vol. 54, no. 3, pp. 852–854, 2015.

[27] J.-F. Cai, X. Qu, W. Xu, and G.-B. Ye, "Robust recovery of complex exponential signals from random Gaussian projections via low rank Hankel matrix reconstruction," *Applied and Com-

*putational Harmonic Analysis*, vol. 41, no. 2, pp. 470–490, 2016.

[28] Y. Wang, A. Szlam, and G. Lerman, "Robust locally linear analysis with applications to image denoising and blind inpainting," *SIAM Journal on Imaging Sciences*, vol. 6, no. 1, pp. 526–562, 2013.

[29] B. Dong, H. Ji, J. Li, Z. Shen, and Y. Xu, "Wavelet frame based blind image inpainting," *Applied and Computational Harmonic Analysis*, vol. 32, no. 2, pp. 268–279, 2012.

[30] S. Boyd, N. Parikh, E. Chu, B. Peleato, and J. Eckstein, "Distributed optimization and statistical learning via the alternating direction method of multipliers," *Found. Trends in Mach. Learn.*, vol. 3, no. 1, pp. 1–122, 2011.

[31] Z. Wen, W. Yin, and Y. Zhang, "Solving a low-rank factorization model for matrix completion by a nonlinear successive over-relaxation algorithm," *Math. Prog. Comp.*, vol. 4, no. 4, pp. 333–361, 2012.

[32] E. J. Candès, X. Li, Y. Ma, and J. Wright, "Robust principal component analysis?" *Journal of the ACM*, vol. 58, no. 3, p. 11, 2011.

[33] J. Wright, A. Y. Yang, A. Ganesh, S. S. Sastry, and Y. Ma, "Robust face recognition via sparse representation," *IEEE Trans. Pattern Anal. Mach. Intell.*, vol. 31, no. 2, pp. 210–227, 2009.

[34] T. F. Chan and J. Shen, "Nontexture inpainting by curvature-driven diffusions," *J. Vision Comm. Image Rep.*, vol. 12, no. 4, pp. 436–449, 2001.

[35] G. R. Cross and A. K. Jain, "Markov random field texture models," *IEEE Trans. Pattern Anal. Mach. Intell.*, no. 1, pp. 25–39, 1983.

[36] E. J. Candes, Y. C. Eldar, T. Strohmer, and V. Voroninski, "Phase retrieval via matrix completion," *SIAM Review*, vol. 57, no. 2, pp. 225–251, 2015.

[37] M. Signoretto, V. Cevher, and J. A. Suykens, "An SVD-free approach to a class of structured low rank matrix optimization problems with application to system identification," in *IEEE Conf. on Decision and Control*, no. EPFL-CONF-184990, 2013.

[38] Z. Zhu, Q. Li, G. Tang, and M. B. Wakin, "Global optimality in low-rank matrix optimization," *arXiv preprint arXiv:1702.07945*, 2017.

[39] G. Harikumar and Y. Bresler, "Exact image deconvolution from multiple FIR blurs," *IEEE Transactions on Image Processing*, vol. 8, no. 6, pp. 846–862, 1999.

[40] S. Ramani and J. Fessler, "Parallel MR image reconstruction using augmented Lagrangian methods," *IEEE Trans. Med. Imag.*, vol. 30, no. 3, pp. 694–706, 2011.

[41] P. Getreuer, "Rudin-Osher-Fatemi total variation denoising using split Bregman," *Image Processing On Line*, vol. 10, 2012.

[42] M. V. Afonso and J. M. R. Sanches, "Blind inpainting using and total variation regularization," *IEEE Transactions on Image Processing*, vol. 24, no. 7, pp. 2239–2253, 2015.

[43] J. Salmon, Z. Harmany, C.-A. Deledalle, and R. Willett, "Poisson noise reduction with non-local pca," *Journal of mathematical imaging and vision*, vol. 48, no. 2, pp. 279–294, 2014.

[44] G. Yu, G. Sapiro, and S. Mallat, "Solving inverse problems with piecewise linear estimators: from Gaussian mixture models to structured sparsity," *IEEE Trans. Image Process.*, vol. 21, no. 5, pp. 2481–2499, 2012.

[45] J. Wright, A. Ganesh, S. Rao, Y. Peng, and Y. Ma, "Robust principal component analysis: Exact recovery of corrupted low-rank matrices via convex optimization," in *Advances in neural information processing systems*, 2009, pp. 2080–2088.

[46] Z. Lin, M. Chen, and Y. Ma, "The augmented lagrange multiplier method for exact recovery of corrupted low-rank matrices," *arXiv preprint arXiv:1009.5055*, 2010.

[47] H. Ji, S. Huang, Z. Shen, and Y. Xu, "Robust video restoration by joint sparse and low rank matrix approximation," *SIAM Journal on Imaging Sciences*, vol. 4, no. 4, pp. 1122–1142, 2011.

[48] W. Dong, G. Shi, and X. Li, "Nonlocal image restoration with bilateral variance estimation: a low-rank approach," *IEEE Trans. Image Process.*, vol. 22, no. 2, pp. 700–711, 2013.

[49] M. Ayazoglu, M. Sznaier, O. Camps *et al.*, "Fast algorithms for structured robust principal component analysis," in *2012 IEEE Conference on Computer Vision and Pattern Recognition (CVPR)*.   IEEE, 2012, pp. 1704–1711.

[50] T. Ding, M. Sznaier, and O. Camps, "Receding horizon rank minimization based estimation with applications to visual tracking," in *2008. 47th IEEE Conference on Decision and Control*. IEEE, 2008, pp. 3446–3451.

[51] R. Yin, T. Gao, Y. Lu, and I. Daubechies, "A tale of two bases: Local-nonlocal regularization on image patches with convolution framelets," *arXiv preprint arXiv:1606.01377*, 2016.
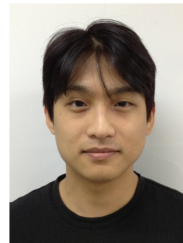
**Kyong Hwan Jin** received the B.S. and the integrated M.S. & Ph.D. degrees from the Department of Bio and Brain Engineering, KAIST - Korea Advanced Institute of Science and Technology, Daejeon, South Korea, in 2008 and 2015, respectively. He was a post doctoral scholar in KAIST from 2015 to 2016. He is currently a post doctoral scholar in Biomedical Imaging Group at the cole Polytechnique Fdrale de Lausanne (EPFL), Switzerland. His research interests include low rank matrix completion, sparsity promoted signal recovery, sampling theory, deep learning, biomedical imaging, and image processing in various applications.

**Jong Chul Ye** joined KAIST, Daejeon, Korea, in 2004, where he is currently KAIST endowed chair professor and a professor of the Dept. of Bio/Brain Engineering and an adjunct professor at Dept. of Mathematical Sciences. He received the B.Sc. and M.Sc. degrees from Seoul National University, Korea, and the Ph.D. from Purdue University, West Lafayette. Before joining KAIST, he worked at Philips Research, and GE Global Research, both in New York. He has served as an Associate Editor of *IEEE Trans. on Image Processing*, and *IEEE Trans. on Computational Imaging*, *Journal of Electronic Imaging*, an editorial board member for *Magnetic Resonance in Medicine*, and an international advisory board for *Physics in Medicine and Biology*. His group was the first place winner of the *2009 Recon Challenge* at the International Society for Magnetic Resonance in Medicine (ISMRM) workshop, and 2nd place winners at *2016 Low Dose CT Grand Challenge* organized by the American Association of Physicists in Medicine (AAPM), and the third place winner for *2017 CVPR NTIRE challenge on example-based single image super-resolution*. He was an advisor of student's best paper awards (first and runner-up) at *2013 and 2016 IEEE Symp. on Biomedical Imaging (ISBI)*. His current research interests include deep learning, compressed sensing, and statistical signal processing for various imaging modalities such as MRI, NIRS, CT, PET, optics, etc.